

# Characterisation of three-body loss in $^{166}\text{Er}$ and optimised production of large Bose–Einstein condensates

Milan Krstajić,\* Péter Juhász,\* Jiří Kučera,\* Lucas R. Hofer, Gavin Lamb, Anna L. Marchant,† and Robert P. Smith‡

*Clarendon Laboratory, University of Oxford, Parks Road, Oxford, OX1 3PU, United Kingdom*

(Dated: 12<sup>th</sup> September, 2023)

Ultracold gases of highly magnetic lanthanide atoms have enabled the realisation of dipolar quantum droplets and supersolids. However, future studies could be limited by the achievable atom numbers and hindered by high three-body loss rates. Here we study density-dependent atom loss in an ultracold gas of  $^{166}\text{Er}$  for magnetic fields below 4 G, identifying six previously unreported, strongly temperature-dependent features. We find that their positions and widths show a linear temperature dependence up to at least 15  $\mu\text{K}$ . In addition, we observe a weak, polarisation-dependent shift of the loss features with the intensity of the light used to optically trap the atoms. This detailed knowledge of the loss landscape allows us to optimise the production of dipolar BECs with more than  $2 \times 10^5$  atoms and points towards optimal strategies for the study of large-atom-number dipolar gases in the droplet and supersolid regimes.

## I. INTRODUCTION

Precise knowledge and control of the nature and strength of interparticle interactions have been a key factor in the success of using degenerate ultracold-atom samples for studying many-body quantum phenomena. The application of a magnetic field close to a Feshbach resonance is a highly versatile and convenient tool for tuning the sign and strength of  $s$ -wave contact interactions that typically dominate in ultracold gases [1]. However, approaching a Feshbach resonance also leads to the enhancement of (detrimental) three-body processes, which result in atom loss and heating [2]. Knowing the location of Feshbach resonances and quantifying the associated loss features is thus essential for designing and optimising ultracold-atom experiments.

The realisation of ultracold samples of highly magnetic erbium [3] and dysprosium atoms [4], which interact via both long-range, anisotropic dipole–dipole interactions and tunable contact interactions, has led to the discovery of dipolar quantum droplets [5–7] and a supersolid phase [8–10], which simultaneously exhibits a global phase order and a spontaneous spatial density modulation. While these first experiments were carried out in cigar-shaped traps leading to (relatively simple) one-dimensional (1D) spatial ordering, more recently droplet arrays and supersolids with two-dimensional (2D) ordering have also been observed [11, 12]. Theoretical works predict a plethora of novel patterns in 2D systems, including so-called honeycomb, labyrinthine and pumpkin phases [13–17]. However, reaching these exotic states requires degenerate samples with higher atom numbers than those used in these experiments so far ( $1.4 \times 10^5$  [10]).

The maximal achievable atom number in an experiment is often restricted by three-body loss processes, which limit the efficiency of evaporative cooling close to degeneracy and can greatly reduce the gas lifetime at (or while approaching) the

desired  $s$ -wave scattering length. Moreover, in order to map out the parameter space of exotic dipolar phases, one needs to tune the relative strength of the contact and dipole–dipole interactions by controlling the strength of the magnetic field. The precise knowledge of the loss landscape as a function of the field strength is therefore paramount. Here we carefully characterise three-body loss in  $^{166}\text{Er}$  for magnetic fields below 4 G, revealing the presence of six previously unreported resonant loss features which display a strong temperature dependence. In light of this, we describe our optimised procedure for the production of  $^{166}\text{Er}$  Bose–Einstein condensates (BECs), containing more than  $2 \times 10^5$  atoms.

## II. THREE-BODY LOSS MEASUREMENTS

In alkali atoms the (number) density of Feshbach resonances is typically between  $0.01 \text{ G}^{-1}$  and  $0.1 \text{ G}^{-1}$  [1]. However, in magnetic lanthanides, including erbium and dysprosium, the anisotropy of the van der Waals and the dipole–dipole interaction potentials leads to coupling between many scattering channels and consequently to an abundance of Feshbach resonances [18–21], some of which show a strong temperature dependence [19, 22, 23]. Here we focus on  $^{166}\text{Er}$  for magnetic fields below 4 G, where Feshbach resonances and associated loss features have been reported at 0.02(5) G, 3.04(5) G and 4.028 G [24].

For our measurements we prepare an ultracold, spin-polarised sample of  $^{166}\text{Er}$  in an (approximately harmonic) optical dipole trap (ODT) formed from 1030 nm laser light. The experimental sequence is described in Sec. III, and the trap and gas parameters for all our loss measurements are given in the Supplemental Material [25]; here we only note that the final stage of cooling is achieved by evaporation in the ODT, with the temperature of the atom cloud controlled by the ODT depth. To produce clouds at different temperatures, we interrupt the normal evaporation sequence at different times and ramp up the depth of the ODT over 100 ms to prevent any further evaporative cooling (and associated atom loss) during our measurements. We initiate the loss measurements by quenching the magnetic field  $B$  [26] to the desired value in  $< 10$  ms. To avoid ramping through wide

\* M. K., P. J. and J. K. contributed equally to this work.

† Present address: STFC Rutherford Appleton Laboratory, Didcot, OX11 0QX, United Kingdom

‡ robert.smith@physics.ox.ac.uk

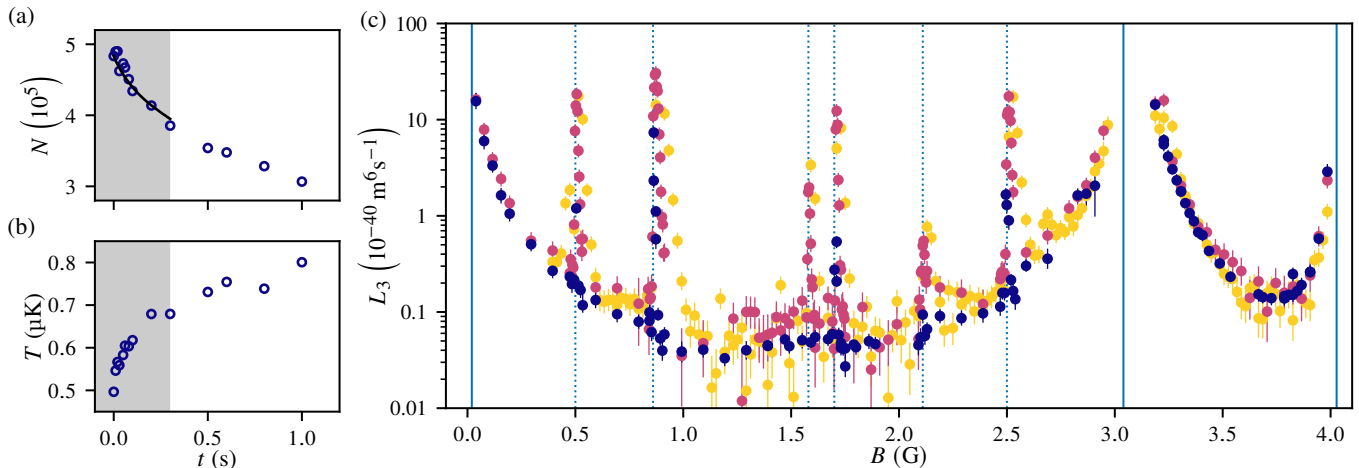


FIG. 1. Three-body loss in  $^{166}\text{Er}$ . (a, b) Time evolution of the atom number  $N$  and temperature  $T$ , respectively, of a thermal cloud of  $^{166}\text{Er}$  atoms at  $B = 2.7$  G with an initial temperature of  $T_i = 0.5$   $\mu\text{K}$ . The shading denotes the region in which  $T$  is within 40% of  $T_i$ ; in this region we fit  $N(t)$  based on Eq. (2) to determine  $L_3$  (solid line, see text). (c) Extracted three-body loss coefficients ( $L_3$ ) for the different initial temperatures  $T_i = \{0.5, 1.5, 4\}$   $\mu\text{K}$  (blue, magenta and yellow points, respectively). In addition to the three previously identified Feshbach resonances (solid vertical lines), we identify six new loss features (dotted vertical lines). These new features show a noticeable temperature dependence; as  $T_i$  increases, the peaks shift to higher  $B$  and their widths also increase.

resonances, for measurements above 3 G we evaporatively cool at 3.8 G, whereas for measurements below 3 G we cool at 1.4 G. We use absorption imaging after a time-of-flight to measure the atom number  $N$  and temperature  $T$  as a function of the time  $t$  the atoms are held in the trap (at a given  $B$ ). Examples of these  $N(t)$  and  $T(t)$  curves are shown in Figs. 1(a) and 1(b); here the initial temperature  $T_i = 0.5$   $\mu\text{K}$  and  $B = 2.7$  G.

Let us first consider atom loss. As the atoms are prepared in the lowest Zeeman state at temperatures much lower than the sub-level splitting ( $\approx 78$   $\mu\text{K G}^{-1}$ ), two-body (spin relaxation) loss processes are energetically suppressed. The evolution of the atom number density in thermal samples can therefore be described by a combination of one- and three-body loss terms [2],

$$\dot{n}(\mathbf{r}) = -\frac{n(\mathbf{r})}{\tau_1} - L_3 n^3(\mathbf{r}), \quad (1)$$

where  $\tau_1$  is the one-body lifetime (set by e.g. collisions with background gas atoms in an imperfect vacuum),  $L_3$  is the three-body loss coefficient and  $n(\mathbf{r})$  is the atom number density. For a thermal cloud (well above the BEC transition temperature), the atomic density distribution in a harmonic trap is Gaussian and Eq. (1) can be written as [2]

$$\frac{\dot{N}}{N} = -\frac{1}{\tau_1} - L_3 \left( \frac{m\bar{\omega}^2}{2\sqrt{3}\pi k_B T} \right)^3 N^2, \quad (2)$$

where  $m$  is the atomic mass,  $\bar{\omega}$  is the geometric mean of the trapping frequencies and  $k_B$  is the Boltzmann constant. The trapping frequencies were measured separately by exciting the cloud centre-of-mass oscillations in the three perpendicular directions and  $\tau_1$  was independently determined to be  $\tau_1 = 33(1)$  s from measurements of low-density clouds for which three-body loss is negligible.

To determine  $L_3(B)$  from our  $N(t)$  measurements, we fit the numerical solution of Eq. (2) to our data [see solid line in Fig. 1(a)] using the corresponding measured  $T(t)$  as an input. We only fit our data within the time interval over which the temperature stays within 40% of its initial value [gray shaded region in Figs. 1(a) and 1(b)] to limit any systematic errors arising from either (i) evaporative atom loss due to the finite trap depth or (ii) the fact that  $L_3$  may depend on  $T$  [27].

Regarding the heating of the atom cloud [Fig. 1(b)], this can be understood to be due to two main processes. First, the loss rate is higher in the central (higher density) part of the trap, preferentially removing atoms with energy lower than the average energy in the cloud, leading to ‘anti-evaporation’ [2]. Second, the products of the three-body collision can have significant kinetic energy (acquired due to the released binding energy when two atoms form a molecule), which may be partially deposited in the cloud via secondary collisions.

Figure 1(c) shows the measured three-body coefficient as a function of the magnetic field for initial temperatures of 0.5  $\mu\text{K}$ , 1.5  $\mu\text{K}$  and 4  $\mu\text{K}$ . In addition to the Feshbach resonances already reported [solid vertical lines in Fig. 1(c)], we observed six additional loss features (dotted vertical lines). These loss features both broaden and shift to higher  $B$  with increasing temperature. We note that at temperatures below 1  $\mu\text{K}$ , where most previous measurements were performed [18, 24], these features become very narrow and can easily be missed.

To explore the temperature dependence further, we measured  $L_3$  as a function of  $B$  around the newly discovered resonance at  $\approx 0.86$  G for several additional  $T_i$  values [see Figs. 2(a)–(c)]. Given the asymmetric shape of the loss features, for each  $T_i$  data series,  $L_3(B)$  was fitted with a heuristic skewed Gaussian

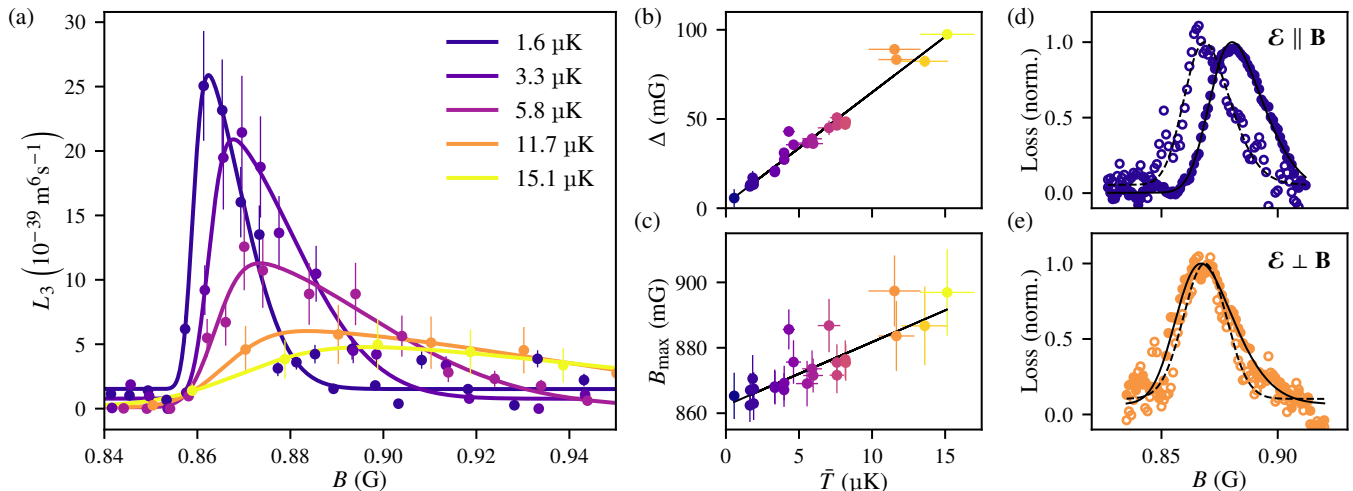


FIG. 2. Temperature dependence and light-shift of the loss feature at  $\approx 0.86$  G. (a)  $L_3$  as a function of  $B$  for several decay series with different  $\bar{T}$ . Markers are experimental data points (with  $L_3$  extracted in the same way as in Fig. 1) and lines are skewed Gaussian fits [see Eq. (3)]. (b) Peak width  $\Delta$  as a function of  $\bar{T}$ . The line is a linear fit to the data and has a slope of  $6.2(3)$  mG  $\mu\text{K}^{-1}$  and an intercept which is consistent with zero. (c) Peak position as a function of  $\bar{T}$ . The linear fit (line) has a slope of  $2.0(3)$  mG  $\mu\text{K}^{-1}$  and an intercept of  $861(1)$  mG. (d, e) Light-shift of the loss resonance for linearly polarised light with the polarisation vector  $\mathcal{E}$  parallel and perpendicular to the dipole orientation, respectively. For both, we plot the normalised loss (see text) for clouds that are prepared at the same temperature ( $2 \mu\text{K}$ ) in 1030 nm single-beam ODTs with a factor of four difference in laser intensity (filled points show the higher intensity); for  $\mathcal{E} \parallel \mathbf{B}$  there is a noticeable light-shift in the resonance position, while the magnitude and width of the feature remains unchanged. Note that the data in (b) and (c) were corrected for this light-shift effect.

curve of the form

$$L_3(B) = A e^{-\frac{(B-B_c)^2}{2\sigma^2}} \left( 1 + \operatorname{erf}\left(\frac{\alpha(B-B_c)}{\sqrt{2}\sigma}\right) \right) + C, \quad (3)$$

where  $B_c$ ,  $\sigma$ ,  $\alpha$ ,  $A$  and  $C$  are fitting parameters.

Figures 2(b) and 2(c) show, respectively, the peak width  $\Delta$  (taken as twice the variance of the skewed Gaussian) and  $B_{\max}$  [the location of the maximum of  $L_3(B)$ ] as a function of the average temperature  $\bar{T}$  of the decay series [28]. We observe that  $\Delta$  grows linearly with temperature and so we parameterise the width of the resonance via a linear function,  $\Delta = \Delta_0 + (d\Delta/dT) \bar{T}$ , fitted to the data [solid line, Fig. 2(b)]. Note that all our extracted  $\Delta_0$  values are consistent with zero within our  $\pm 3$  mG error bounds. Similarly,  $B_{\max}$  also grows (approximately) linearly with temperature and so we fit the data using  $B_{\max} = B_0 + (dB_{\max}/dT) \bar{T}$ . The parameters of both these fits are tabulated in Table I for all the newly detected loss features. We also note that for the 0.86 G feature the maximum  $L_3$  decreases with increasing temperature within our measured range [see Fig. 2(a)], however, for other peaks this trend is inconclusive.

The magnetic field dependence of the loss properties is due to the differential Zeeman shift arising from the difference in magnetic moments ( $\delta\mu$ ) between the different scattering channels. However, it is also possible for light fields to exert similar differential shifts [29–32] due to the difference in polarisabilities ( $\delta\alpha$ ) between scattering channels, which can, in some cases, also have vectorial and tensorial parts [33, 34]. To check if the optical field from our ODT causes such an effect, we measured the loss features for thermal clouds at

the same temperature ( $2 \mu\text{K}$ ) but for traps with two different light intensities (powers) and for the polarisation of the ODT light  $\mathcal{E}$  either parallel ( $\mathcal{E} \parallel \mathbf{B}$ ) or perpendicular ( $\mathcal{E} \perp \mathbf{B}$ ) to the external magnetic field (and hence the spin-polarisation of the atoms) [35]. Data for the 0.86 G resonance is shown in Figs. 2(d) and 2(e); here, to identify the peak position we simply performed a two-point loss measurement [36]. For  $\mathcal{E} \parallel \mathbf{B}$  we observe a significant (positive) shift of the loss feature with light intensity, whereas for  $\mathcal{E} \perp \mathbf{B}$  the effect is much less noticeable and (if anything) has the opposite sign. Assuming

$B_0$ (mG)	$\frac{dB_{\max}}{dT}$ (mG $\mu\text{K}^{-1}$ )	$\frac{d\Delta}{dT}$ (mG $\mu\text{K}^{-1}$ )	$\left(\frac{dB_0}{dI}\right)_{\mathcal{E} \parallel \mathbf{B}}$ (G $\mu\text{m}^2 \text{W}^{-1}$ )	$\left(\frac{dB_0}{dI}\right)_{\mathcal{E} \perp \mathbf{B}}$ (G $\mu\text{m}^2 \text{W}^{-1}$ )
498(2)	3.0(4)	8.6(2.2)	1.5(3)	-0.5(2)
862(2)	1.9(3)	6.2(3)	1.7(5)	-0.2(2)
1571(4)	4.3(7)	4.6(1.5)	0.7(2)	0.1(3)
1705(3)	2.7(7)	5.3(1.0)	1.2(6)	-0.1(3)
2102(3)	5.6(7)	7.8(8)	2.6(9)	0.1(9)
2497(7)	3.8(1.6)	6.1(5)	1.9(3)	0.0(4)

Table I. Newly detected loss features and their properties. The position of the resonance  $B_0$  for  $T \rightarrow 0$  (and  $I \rightarrow 0$ ) and the rate of change of the peaks' position ( $dB_{\max}/dT$ ) and width ( $d\Delta/dT$ ) with temperature, obtained via a linear fit to the finite-temperature datasets. The shift in the resonance position with the intensity of linearly polarised 1030 nm laser light ( $dB_0/dI$ ) is also tabulated, for dipoles aligned along ( $\mathcal{E} \parallel \mathbf{B}$ ) and perpendicular to ( $\mathcal{E} \perp \mathbf{B}$ ) the light polarisation.

that the resonance position shifts linearly with light intensity, one can extract a constant of proportionality between the light intensity  $I$  and the resonance peak shift which gives  $dB_0/dI$  for both orientations. These are tabulated in Table I for all the newly detected loss features.

We note that, for all the loss features, the fact that the difference in the slopes  $dB_0/dI$  between the two orthogonal light polarisations is of similar magnitude to either of the individual slopes suggests that the tensorial part of  $\delta\alpha$  is of a similar magnitude to its scalar part. More quantitatively, using  $\delta\alpha = 2\varepsilon_0 c \delta\mu dB_0/dI$ , we find  $\delta\alpha \sim 1$  a.u. using  $\delta\mu \sim \mu_B$ , which is the same order of magnitude as the tensorial part of the ground state polarisability at the wavelength of our ODT [33].

We now compare our findings to the predictions of a ‘resonant trimer’ model previously proposed in the context of temperature-dependent loss features in the lanthanides [19]. In this model the loss features are caused by resonances with ‘closed channel’ three-atom (trimer) bound states. We note that as the resonance is with a trimer (rather than a two-atom bound state as in more conventional Feshbach resonances), one would not expect these resonances to affect the (two-body)  $s$ -wave scattering length [37].

Within this model, some simple scalings emerge for  $k_B T \gg \Gamma_{\text{br}} \gg \Gamma(E)$ , where  $\Gamma_{\text{br}}$  is the trimer decay rate (into an atom and dimer pair) and  $\Gamma(E)$  is the collision energy dependent width of the trimer resonance. In this regime, one finds that  $B_{\text{max}} - B_0 = (\lambda + 2)k_B T / \delta\mu$ ,  $\Delta = 2\sqrt{3 + \lambda}k_B T / \delta\mu$  and  $L_3(B_{\text{max}}) \propto T^{\lambda-1}$ , where  $\lambda$  is related to the orbital angular momentum of the entrance channel ( $\lambda = 0, 2$  for  $s$ -wave and  $d$ -wave respectively).

The first thing to note is the qualitative agreement between these predictions and our observed temperature dependencies of  $B_{\text{max}}$  and  $\Delta$ . More quantitatively, the ratio of  $d\Delta/dT$  and  $dB_{\text{max}}/dT$  is predicted to only depend on  $\lambda$  and be equal to 1.73 and 1.12 for  $\lambda = 0$  and 2, respectively. For the 0.86 G resonance this ratio is 3.2(5), which is closer to the  $s$ -wave prediction [38]. An  $s$ -wave assignment would also be consistent with the fact that the maximum  $L_3$  drops with temperature. For the other resonances, the larger error bars and the inconclusive trends of  $L_3(B_{\text{max}})$  against  $T$  make any  $\lambda$  assignment difficult.

Finally, we note that, despite the consistency of the 0.86 G feature with the resonant trimer model, we cannot rule out alternative models [22] which also predict regimes with linear  $T$ -dependence of both  $B_{\text{max}}$  and  $\Delta$ , especially for the other less well-mapped loss features.

### III. OPTIMISED BEC PRODUCTION

To produce erbium BECs, we employ standard laser cooling and trapping techniques and then use our knowledge of  $L_3(B)$  to inform and optimise the evaporative cooling sequence.

In the initial steps, similarly to Ref. [3], an atomic beam emerging from a high-temperature effusion cell oven is slowed down using a Zeeman slower operating on the broad transition at 401 nm. The slow atoms are then loaded into a narrow-line magneto-optical trap (MOT) operating on the atomic transition at 583 nm. We typically capture  $10^8$  atoms after

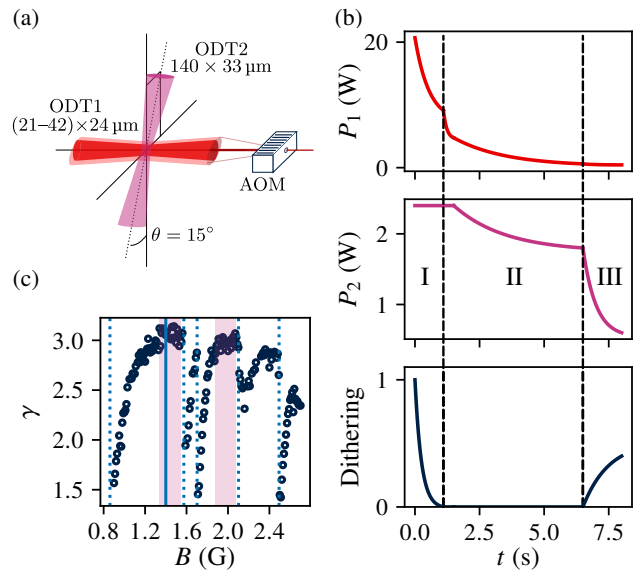


FIG. 3. Optimising evaporation. (a) Schematics of the crossed-beam optical dipole trap. The horizontal (ODT1) beam can be enlarged by dithering it with an AOM. The cross (ODT2) beam propagates at  $15^\circ$  to the vertical. (b) After loading the ODT from the cMOT, the evaporation sequence consists of three parts. During phase I, the power in ODT1 is lowered in parallel with ramping down the dithering. In phase II, the atoms are drawn into the crossing with the second ODT beam as the cooling continues. Finally, in phase III, with atoms residing entirely in the crossed region, we decompress the trap by ramping down ODT2 and dithering the ODT1 beam.  $P_1$  and  $P_2$  correspond to the power in ODT1 and ODT2, respectively, and the dithering amplitude is shown in arbitrary units. (c) Evaporation efficiency  $\gamma$  (see text) as a function of magnetic field. The dashed vertical lines show the  $T \rightarrow 0$  positions of the loss features. The shaded regions denote optimal regions for evaporation and  $B = 1.4$  G, which we use during evaporation, is indicated by a solid vertical line.

loading the MOT for 12 s. Afterwards, we ramp to a compressed MOT (cMOT) configuration in 600 ms, where reducing the light detuning and intensity causes simultaneous compression and cooling, resulting in a spin-polarised atomic sample at a temperature of  $10 \mu\text{K}$ .

To cool the sample further, we transfer the atoms into an ODT, broadly following previous protocols, in which we perform evaporative cooling. As shown in Fig. 3(a), the ODT is implemented using two crossed, far-detuned beams at 1030 nm, which we call ODT1 and ODT2. Initially, the  $21 \mu\text{m} \times 24 \mu\text{m}$  waist ODT1 beam is superimposed onto the cMOT, with a total power of 21 W and with a 50 kHz spatial dithering applied using an acousto-optic modulator (AOM) [39], which broadens the horizontal ( $21 \mu\text{m}$ ) waist by a factor of two. A 40 ms overlap of the dithered ODT1 beam with the cMOT results in  $1.8 \times 10^7$  atoms being trapped in ODT1 at a temperature of  $\approx 40 \mu\text{K}$ .

The next step is to evaporatively cool the atoms; it is here where a consideration of three-body losses becomes important. Maximising the evaporation efficiency requires minimising losses while still maintaining a sufficient rate of elastic two-body collisions which facilitate evaporation. To minimise three-body losses in the range of temperatures encountered during

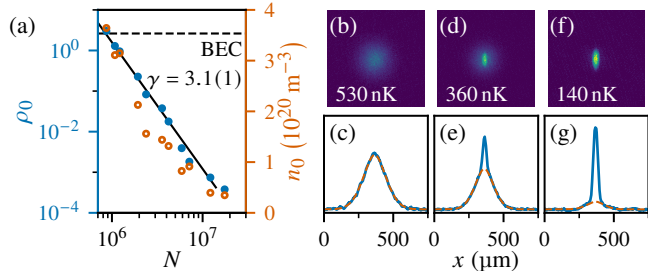


FIG. 4. Evaporation to BEC. (a) Evolution of the peak phase-space density ( $\rho_0$ , blue circles) and number density ( $n_0$ , orange circles) with the total atom number ( $N$ ) during evaporation. A linear fit on the logarithmic plot shows that  $\gamma = -d(\ln \rho_0)/d(\ln N) = 3.1(1)$ . (b–f) Time-of-flight absorption images and summed density plots of atomic clouds: (b, c) just prior to condensation, corresponding to the highest  $\rho_0$  point in (a), (d, e) a partially condensed cloud, (f, g) a nearly pure BEC with  $2.2 \times 10^5$  atoms in the condensate. The dashed line in the summed density plots represents a fit of the extended Bose distribution to the thermal component of the cloud, from which the temperature can be extracted.

evaporation, one wants to be roughly in the middle of the range between the two (relatively broad) Feshbach resonances at 0 G and 3 G. Additionally, one wants to be as far as possible to the high-field side of any of the loss features, as they both move and broaden towards higher  $B$  as  $T$  increases. This points towards choosing  $B \approx 1.5$  G, on the right of the largest gap between loss features [see Fig. 1(c)]. On the other hand, the elastic collision rate, set by the  $s$ -wave scattering length  $a_s$ , increases as one approaches the 3 G resonance from below [24]. This favours higher  $B$  and points towards the regions around 2 G and 2.4 G.

To discern the optimal  $B$  for evaporation, in Fig. 3(c) we plot the efficiency ( $\gamma$ ) of the evaporation ramp down to the point just above condensation as a function of  $B$ . Here  $\gamma = -d(\ln \rho_0)/d(\ln N)$ , where  $\rho_0 = n_0 \lambda_T^3$  is the peak phase-space density with  $\lambda_T = \sqrt{2\pi\hbar^2/mk_B T}$  the thermal de Broglie wavelength. We see that there is indeed an optimal region around  $B = 1.4$  G and so we perform our evaporation there, at which point  $a_s = 73a_0$  [24]. We note that the region around 2 G is also suitable for evaporation, as although it suffers from greater three-body loss, it has a larger  $a_s \approx 80a_0$ . This observation is consistent with the 1.9 G field used previously for evaporation (see the supplemental material of Ref. [10]).

The evaporation sequence can be split into three stages [see Fig. 3(b)]. In stage I, in which the ODT2 contributes negligibly to the trapping, we simultaneously reduce the ODT1 power and ramp down its dithering. This leads to evaporation and a change in the trap aspect ratio, but avoids too much decompression. At the start of stage II, the ODT2 beam, with a waist of  $140 \mu\text{m} \times 33 \mu\text{m}$  and an initial power of 2.4 W, starts to have a noticeable effect and, as the cooling continues, the remaining atoms converge into the crossing of the ODT beams.

In stage III, we employ the novel approach of broadening the ODT1 beam again by ramping up the dithering amplitude alongside significantly decreasing the power of ODT2. This lowers the trap depth and all trapping frequencies, and thereby reduces the atomic density and hence the rate of inelastic three-body collisions relative to the elastic two-body ones.

In Fig. 4(a) we show how the peak density  $n_0$  and the peak phase-space density  $\rho_0$  evolve with the falling  $N$  during the evaporation sequence. This highlights the growing density and justifies the need for our stage III decompression: at the end of stage II we reach  $n_0 = 3 \times 10^{20} \text{ m}^{-3}$  which gives a characteristic three-body lifetime at the centre of the cloud of only  $1/L_3 n_0^2 \approx 1$  s. We achieve efficient evaporation throughout the three stages, maintaining a steady increase of  $\rho_0$  with efficiency  $\gamma = 3.1(1)$ ; this results in the onset of condensation being reached with  $N = 8 \times 10^5$  atoms and at a temperature of 500 nK. Finally, by evaporating further we achieve a nearly pure condensate with  $2.2 \times 10^5$  atoms [see Figs. 4(b)–(g)].

#### IV. CONCLUSION

In conclusion, we have identified six new strongly temperature-dependent three-body loss features in  $^{166}\text{Er}$  below 4 G. Both the position and width of these loss features increase linearly with temperature for  $0.5 < T < 15 \mu\text{K}$ ; this is broadly consistent with a ‘resonant trimer’ model previously put forward to explain some loss features in lanthanide atoms [19].

Using our knowledge of the loss landscape to optimise the evaporation procedure enabled the production of large BECs of  $2.2 \times 10^5$  atoms, providing a good starting point for the investigation of ultracold dipolar physics. Furthermore, these findings will enable the optimisation of atom numbers in existing and future experiments, and guide the way towards the experimental realisation of more exotic states, including honeycomb, labyrinthine and pumpkin phases. Moreover, precise knowledge of the three-body loss coefficient could enable the measurement of the atom number density, crucial for determining the structure of quantum droplets.

#### ACKNOWLEDGMENTS

We thank Nathaniel Vilas for contributions to the early stages of the experiment, and Raphael Lopes and Jean Dalibard for useful discussions. This work was supported by the UK EPSRC (grants no. EP/P009565/1 and EP/T019913/1). R. P. S. and P. J. acknowledge support from the Royal Society, P. J. acknowledges support from the Hungarian National Young Talents Scholarship, M. K. from Trinity College, Cambridge, J. K. from the Oxford Physics Endowment for Graduates (OXPEG) and G. L. from Wolfson College, Oxford.

[1] C. Chin, R. Grimm, P. Julienne, and E. Tiesinga, Feshbach resonances in ultracold gases, *Rev. Mod. Phys.* **82**, 1225 (2010).

[2] T. Weber, J. Herbig, M. Mark, H.-C. Nägerl, and R. Grimm,

- Three-Body Recombination at Large Scattering Lengths in an Ultracold Atomic Gas, *Phys. Rev. Lett.* **91**, 123201 (2003).
- [3] K. Aikawa, A. Frisch, M. Mark, S. Baier, A. Rietzler, R. Grimm, and F. Ferlaino, Bose-Einstein Condensation of Erbium, *Phys. Rev. Lett.* **108**, 210401 (2012).
- [4] M. Lu, N. Q. Burdick, S. H. Youn, and B. L. Lev, Strongly Dipolar Bose-Einstein Condensate of Dysprosium, *Phys. Rev. Lett.* **107**, 190401 (2011).
- [5] H. Kadau, M. Schmitt, M. Wenzel, C. Wink, T. Maier, I. Ferrier-Barbut, and T. Pfau, Observing the Rosensweig instability of a quantum ferrofluid, *Nature* **530**, 194 (2016).
- [6] I. Ferrier-Barbut, H. Kadau, M. Schmitt, M. Wenzel, and T. Pfau, Observation of Quantum Droplets in a Strongly Dipolar Bose Gas, *Phys. Rev. Lett.* **116**, 215301 (2016).
- [7] L. Chomaz, S. Baier, D. Petter, M. J. Mark, F. Wächtler, L. Santos, and F. Ferlaino, Quantum-Fluctuation-Driven Crossover from a Dilute Bose-Einstein Condensate to a Macrodroplet in a Dipolar Quantum Fluid, *Phys. Rev. X* **6**, 041039 (2016).
- [8] F. Böttcher, J.-N. Schmidt, M. Wenzel, J. Hertkorn, M. Guo, T. Langen, and T. Pfau, Transient Supersolid Properties in an Array of Dipolar Quantum Droplets, *Phys. Rev. X* **9**, 011051 (2019).
- [9] L. Tanzi, S. M. Rocuzzo, E. Lucioni, F. Famà, A. Fioretti, C. Gabbanini, G. Modugno, A. Recati, and S. Stringari, Supersolid symmetry breaking from compressional oscillations in a dipolar quantum gas, *Nature* **574**, 382 (2019).
- [10] L. Chomaz, D. Petter, P. Ilzhöfer, G. Natale, A. Trautmann, C. Politi, G. Durastante, R. M. W. van Bijnen, A. Patscheider, M. Sohmen, M. J. Mark, and F. Ferlaino, Long-Lived and Transient Supersolid Behaviors in Dipolar Quantum Gases, *Phys. Rev. X* **9**, 021012 (2019).
- [11] M. A. Norcia, C. Politi, L. Klaus, E. Poli, M. Sohmen, M. J. Mark, R. N. Bisset, L. Santos, and F. Ferlaino, Two-dimensional supersolidity in a dipolar quantum gas, *Nature* **596**, 357 (2021).
- [12] T. Bland, E. Poli, C. Politi, L. Klaus, M. A. Norcia, F. Ferlaino, L. Santos, and R. N. Bisset, Two-Dimensional Supersolid Formation in Dipolar Condensates, *Phys. Rev. Lett.* **128**, 195302 (2022).
- [13] D. Baillie and P. B. Blakie, Droplet Crystal Ground States of a Dipolar Bose Gas, *Phys. Rev. Lett.* **121**, 195301 (2018).
- [14] Y.-C. Zhang, T. Pohl, and F. Maucher, Phases of supersolids in confined dipolar Bose-Einstein condensates, *Phys. Rev. A* **104**, 013310 (2021).
- [15] J. Hertkorn, J.-N. Schmidt, M. Guo, F. Böttcher, K. S. H. Ng, S. D. Graham, P. Uerlings, T. Langen, M. Zwierlein, and T. Pfau, Pattern formation in quantum ferrofluids: From supersolids to superglasses, *Phys. Rev. Res.* **3**, 033125 (2021).
- [16] J. Hertkorn, J.-N. Schmidt, M. Guo, F. Böttcher, K. S. H. Ng, S. D. Graham, P. Uerlings, H. P. Büchler, T. Langen, M. Zwierlein, and T. Pfau, Supersolidity in Two-Dimensional Trapped Dipolar Droplet Arrays, *Phys. Rev. Lett.* **127**, 155301 (2021).
- [17] E. Poli, T. Bland, C. Politi, L. Klaus, M. A. Norcia, F. Ferlaino, R. N. Bisset, and L. Santos, Maintaining supersolidity in one and two dimensions, *Phys. Rev. A* **104**, 063307 (2021).
- [18] A. Frisch, M. Mark, K. Aikawa, F. Ferlaino, J. L. Bohn, C. Makrides, A. Petrov, and S. Kotochigova, Quantum chaos in ultracold collisions of gas-phase erbium atoms, *Nature* **507**, 475 (2014).
- [19] T. Maier, H. Kadau, M. Schmitt, M. Wenzel, I. Ferrier-Barbut, T. Pfau, A. Frisch, S. Baier, K. Aikawa, L. Chomaz, M. J. Mark, F. Ferlaino, C. Makrides, E. Tiesinga, A. Petrov, and S. Kotochigova, Emergence of Chaotic Scattering in Ultracold Er and Dy, *Phys. Rev. X* **5**, 041029 (2015).
- [20] K. Baumann, N. Q. Burdick, M. Lu, and B. L. Lev, Observation of low-field Fano-Feshbach resonances in ultracold gases of dysprosium, *Phys. Rev. A* **89**, 020701(R) (2014).
- [21] V. A. Khlebnikov, D. A. Pershin, V. V. Tsyganok, E. T. Davletov, I. S. Cojocar, E. S. Fedorova, A. A. Buchachenko, and A. V. Akimov, Random to Chaotic Statistic Transformation in Low-Field Fano-Feshbach Resonances of Cold Thulium Atoms, *Phys. Rev. Lett.* **123**, 213402 (2019).
- [22] Q. Beaufils, A. Crubellier, T. Zanon, B. Laburthe-Tolra, E. Maréchal, L. Vernac, and O. Gorceix, Feshbach resonance in  $d$ -wave collisions, *Phys. Rev. A* **79**, 032706 (2009).
- [23] V. A. Khlebnikov, V. V. Tsyganok, D. A. Pershin, E. T. Davletov, E. Kuznetsova, and A. V. Akimov, Characterizing the temperature dependence of Fano-Feshbach resonances of ultracold polarized thulium, *Phys. Rev. A* **103**, 023306 (2021).
- [24] A. Patscheider, L. Chomaz, G. Natale, D. Petter, M. J. Mark, S. Baier, B. Yang, R. R. W. Wang, J. L. Bohn, and F. Ferlaino, Determination of the scattering length of erbium atoms, *Phys. Rev. A* **105**, 063307 (2022), the authors of that work confirmed that the location of the highest resonance is 4.028 G and not 4.208 G, as can be seen from Fig. 3 of that work (private communication).
- [25] See Supplemental Material for ODT powers, polarisations and associated trap frequencies, the average temperatures and initial atom numbers for all the data series used in Figs. 1 and 2.
- [26] The magnetic field is calibrated to an accuracy of 1 mG using radio frequency (RF) spectroscopy within the ground state Zeeman manifold. However, the quoted magnetic fields are also affected by an error of  $\pm 5$  mG between different datasets, due to long-term drifts between RF measurements.
- [27] The 40% cutoff is chosen as a tradeoff between minimising systematic errors (with a lower cutoff) and random errors (by choosing a higher cutoff to include more data).
- [28] Note that the average temperature of a decay series  $\bar{T}$  is up to 20% higher than the  $T_i$  for the same series due to the heating associated with the three-body loss.
- [29] D. M. Bauer, M. Lettner, C. Vo, G. Rempe, and S. Dürr, Combination of a magnetic Feshbach resonance and an optical bound-to-bound transition, *Phys. Rev. A* **79**, 062713 (2009).
- [30] Z. Fu, P. Wang, L. Huang, Z. Meng, H. Hu, and J. Zhang, Optical control of a magnetic Feshbach resonance in an ultracold Fermi gas, *Phys. Rev. A* **88**, 041601(R) (2013).
- [31] M. Cetina, M. Jag, R. S. Lous, J. T. M. Walraven, R. Grimm, R. S. Christensen, and G. M. Bruun, Decoherence of Impurities in a Fermi Sea of Ultracold Atoms, *Phys. Rev. Lett.* **115**, 135302 (2015).
- [32] L. W. Clark, L.-C. Ha, C.-Y. Xu, and C. Chin, Quantum Dynamics with Spatiotemporal Control of Interactions in a Stable Bose-Einstein Condensate, *Phys. Rev. Lett.* **115**, 155301 (2015).
- [33] J. H. Becher, S. Baier, K. Aikawa, M. Lepers, J.-F. Wyart, O. Dulieu, and F. Ferlaino, Anisotropic polarizability of erbium atoms, *Phys. Rev. A* **97**, 012509 (2018).
- [34] T. Chalopin, V. Makhalov, C. Bouazza, A. Evrard, A. Barker, M. Lepers, J.-F. Wyart, O. Dulieu, J. Dalibard, R. Lopes, and S. Nascimbene, Anisotropic light shift and magic polarization of the intercombination line of dysprosium atoms in a far-detuned dipole trap, *Phys. Rev. A* **98**, 040502(R) (2018).
- [35] Note that for linearly polarised light, there is no vector component of the polarisability [33] and so the angle between  $\mathbf{B}$  and the direction of propagation of the light does not matter.
- [36] In our two-point measurements the loss is  $N(0) - N(t_{\text{hold}})$ , where  $t_{\text{hold}}$  is a fixed hold time, the peak loss is then normalised to 1.
- [37] Consistent with this, we note that we found no significant change of the cross-thermalisation rate across the 0.86 G resonance.
- [38] Note that as the assumption  $\Gamma_{\text{br}} \gg \Gamma(E)$  weakens, we numerically found that while the linear  $T$ -dependence of  $B_{\text{max}}$  and  $\Delta$  still

approximately hold, the ratio of the gradients becomes larger.

[39] C. Kohstall, *A New Toolbox for Experiments with Ultracold  ${}^6\text{Li}$* , Master's thesis, University of Innsbruck (2007).